NANO · MICRO small
www.small-journal.com

High-Performance Potassium-Tellurium Batteries Stabilized by Interface Engineering

*Yue Zhang, Hongzheng Zhu, Donald J. Freschi, and Jian Liu**

The emerging potassium-tellurium (K-Te) battery system is expected to realize fast reaction kinetics and excellent rate performance due to the exceptional electrical conductivity of Te. However, there has been a lack of fundamental knowledge about this new K-Te system, including the reaction mechanism and cathode structure design. Herein, a two-step reaction pathway from Te to K_2Te_3 and ultimately to K_5Te_3 is investigated in carbonate electrolyte-based K-Te batteries by X-ray diffraction, high-resolution transmission electron microscopy, and selected area electron diffraction characterizations. Additionally, the atomic layer deposition technique is adopted to deposit an ultrathin aluminum oxide (Al_2O_3) film on the electrode surface, which induces the generation of a stable solid electrolyte interphase layer and reduces the loss of active materials effectively. Consequently, the rationally fabricated Te/porous carbon cathode with functional Al_2O_3 coating delivers remarkable long-term cycling stability over 500 cycles at 1 C with an ultralow capacity decay of only 0.01% per cycle. This interface engineering strategy is validated to stabilize the electrode surface, enhance the structural integrity and ensure reliable electron transfer and K-ion conduction over repeated potassiation/depotassiation cycles. These findings are expected to promote the development of high-energy-density K-S/Se/Te batteries.

1. Introduction

Nowadays, lithium-ion batteries (LIB) have been widely applied in portable electronics, electric vehicles, and renewable energy storage due to their merits of high energy density, long lifetime, and fast response.[1–3] However, the uneven distribution and limited lithium resources raise concerns about whether LIB can offer an increasingly growing power supply for large-scale energy storage.[4–6] Potassium-ion batteries (PIB) are considered as a potential alternative for LIB owing to the abundance and low cost of potassium resources and low redox potential for K/K^+ (–2.93 V versus standard hydrogen potential).[7] These advantages have promoted a fast research development of PIB over the past few years, primarily focusing on anode/cathode materials and electrolyte design.[8–14]

Currently, high-voltage (2–4 V) cathode materials are receiving intense attention,[15] such as Prussian blue analogues,[16] layered metal oxides,[9,17,18] polyanionic compounds,[19] and organic cathodes.[20,21] One big challenge of these cathodes is the relatively low capacity of less than 180 mAh g^{-1}, which drags down the overall energy density of a full cell.[22] Conversion-type sulfur (S) or selenium (Se) is expected to realize a high theoretical capacity of 1675 and 675 mAh g^{-1}, respectively.[23–25] However, the newly emerging K-S or K-Se batteries deliver unsatisfying capacity far away from their ideal value in practical applications, which was mainly caused by the dissolution of polysulfies/polyselenides intermediates and poor electrical conductivity of S (5×10^{-28} S cm^{-1}) and Se (5×10^{-3} S cm^{-1}).[26,27] Poor electric conductivity results in sluggish reaction kinetics, low utilization of active materials, severe capacity decay, and unsatisfying rate performance.[28,29]

Tellurium (Te), another chalcogen element, possesses an excellent electrical conductivity of 2×10^2 S cm^{-1} and a high volumetric capacity of 2621 mAh cm^{-3} (specific capacity of 420 mAh g^{-1}), showing great potential as cathode materials for lithium/sodium-ion storage.[30,31] Sun et al.[32] pioneered the study of Te cathodes in PIB with an average potential of 1.6 V in 2020. They revealed a stepwise reaction mechanism ($Te \leftrightarrow K_2Te_3 \leftrightarrow K_5Te_3$) in the ether-based electrolyte (KTFSI in DEGDME). The major issues for this K-Te battery system were low discharge capacity and rapid capacity fading, probably caused by the large volume change of Te and the dissolution of polytellurides during cycling.[33,34] By increasing electrolyte concentration from 1 M to 5 M KTFSI in DEGDME, the battery delivered a higher capacity up to 409 mAh g^{-1}. However, severe capacity decay still occurred, which requires rational cathode structure design to confine the acute volume change of Te. Guo et al.[35] disclosed the K-ion storage mechanism of Te cathode in the carbonate-based electrolyte (1 M KFSI in EC:DEC) with K_2Te as the final potassiation product via a two-electron reaction ($2\,K + Te \leftrightarrow K_2Te$). The excellent cycling stability was achieved with a specific capacity of 215.5 mAh g^{-1} after 100 cycles at 5C due to the superb immobilization of Te nanoparticles on the

Y. Zhang, H. Zhu, J. Liu
School of Engineering
Faculty of Applied Science
The University of British Columbia
3333 University Way
Kelowna, BC V1V 1V7, Canada
E-mail: Jian.liu@ubc.ca
D. J. Freschi
Fenix Advanced Materials
2950 Highway Drive, Trail, BC V1R 2T3, Canada
The ORCID identification number(s) for the author(s) of this article can be found under https://doi.org/10.1002/smll.202200085.

DOI: 10.1002/smll.202200085

G-CNT matrix. On the other hand, Liu et al.[36] reported an enhanced K-Te battery via rational design and electrolyte chemistry. Potassium hexafluorophosphate (KPF_6) was found to facilitate electron transfer and K-ion diffusion, thus boosting redox kinetics and K-ion storage performance. Potassium bis(fluorosulfonyl)imide (KFSI) was found to induce a KF-rich solid electrolyte interphase (SEI) layer on the Te electrode surface and hence suppress side reactions and improve Coulombic efficiency. Nevertheless, the K-Te battery is still a new system that requires more fundamental understanding and exploration.

In this work, a K-Te battery is designed with Te confined into porous carbon (BP2000) as cathode materials. This battery delivers two charge/discharge plateaus in carbonate-based electrolyte corresponding to the stepwise phase transformation from Te to K_2Te_3 and ultimately to K_5Te_3, which is confirmed by the characterizations of X-ray diffraction (XRD), high-resolution transmission electron microscopy (HRTEM), and selected area electron diffraction (SAED). More importantly, the capacity decline issue, caused by the large volume change of Te, is addressed by precisely depositing ultrathin Al_2O_3 film on electrode surface via atomic layer deposition (ALD) technique. With the help of the Al_2O_3 layer, the Te/C cathode shows superior cycling stability, and the capacity decay is as low as only 0.01% per cycle over 500 cycles at 1C. It is expected that the proposed strategies will stimulate more research in the development of durable and high-capacity K-chalcogen (S/Se/Te) batteries.

2. Results and Discussion

Previous studies showed that the phase transformation from Te to K_2Te during the discharge process accompanied massive volume expansion (398%).[35] The undesirable volume change causes pulverization of Te active materials and irreversible capacity loss.[34,37] Herein, porous carbon BP2000 is utilized as the Te host via the melt diffusion method to effectively confine Te during the potassiation/depotassiation process.[38] Scanning electron microscopy (SEM) images in **Figure 1**a shows irregular shapes of BP2000 powders. BP2000 consists of a majority of micropores below 2 nm and a small portion of mesopores with a pore size of 3 nm, as indicated by the hysteresis at high relative pressure above 0.9 in the pore size distribution (Figure 1b). Figure 1c demonstrates the characteristics of both type II and type IV isotherms of BP2000, confirming that BP2000 possesses mixed micropores and mesopores. The large surface area of 1515.7 $m^2\ g^{-1}$ and pore volume of 2.45 $cm^3\ g^{-1}$ can offer sufficient Te loading sites to confine Te and accommodate its volume change. After incorporating Te, Te/BP2000 shows no significant difference in the SEM images (Figure 1d) compared to BP2000. By characterizing Te/BP2000 composite at the nanometer level by transmission electron microscopy (TEM), abundant dark particles are observed (Figure 1e), implying a successful infusion of Te into micro/mesopores. HRTEM images in Figure 1f,g illustrate amorphous structure in most areas and a small proportion of ordered planes. The interplanar distance of 0.32 nm is assigned to the (011) plane of crystalline Te. The SAED inset in Figure 1g also proves the existence of crystalline Te. High-angle annular dark field (HAADF) and energy dispersive X-ray spectroscopy (EDS) mapping in Figure 1h suggest the uniform distribution of Te in the BP2000 matrix. XRD pattern of Te/BP2000 composite in Figure 1i demonstrates only one broad characteristic peak of Te at 27.6° agreeing with the (011) plane of Te (JCPDS PDF # 79-0736). Based on these results, Te is wholly impregnated into porous carbon BP2000 in the existence of dominant amorphous Te and minor crystalline Te.

The electrochemical performance of Te/BP2000 is evaluated in a K-Te cell at various current densities from 0.1 to 10 A g^{-1}. S/BP2000 and Se/BP2000 cathodes are also prepared by the same melt diffusion method and slurry casting process and tested at the same current density and voltage range (0.5–3 V) for a fair comparison. The broad XRD patterns of S/BP2000 and Se/BP2000 in Figure S1 (Supporting Information) imply the impregnation of S and Se into carbon pores. Figure S2 (Supporting Information) confirms active materials contents in the cathodes, i.e., 54 wt% S in S/BP2000, 52 wt% Se in Se/BP2000, and 46 wt% Te in Te/BP2000. **Figure 2**a–c shows galvanostatic charge/discharge profiles of S/BP2000, Se/BP2000, and Te/BP2000 cathodes, respectively. The specific capacity is calculated based on the mass of active materials (S, Se, or Te). In the first potassiation process at 0.1 A g^{-1}, S/BP2000, Se/BP2000, and Te/BP2000 cathodes deliver a specific capacity of 1442.5, 1026.7, and 1180.5 mAh g^{-1}, respectively. The multiple discharge platforms for S/BP2000 and Se/BP2000 could be attributed to the formation of polysulfides and polyselenides,[39,40] which are also observed from several oxidation/reduction peaks in the 1st cyclic voltammetry (CV) scan (Figure S3, Supporting Information). The irreversible capacity between the 1st and 2nd cycles is due to the decomposition of electrolytes, the formation of solid electrolyte interphase (SEI), and irreversible capacity contribution from the carbon host.[25,41] The capacity contribution of BP2000 carbon is presented in Figure S4 (Supporting Information). BP2000 delivered a high initial capacity of 637 mAh g^{-1} followed by a fast decline to 100 mAh g^{-1}, suggesting high irreversible capacity from the BP2000 carbon host. Moreover, it should be noted that, due to the mass ratio of Te/BP2000 (54:46), BP2000 only contributed to 46 mAh g^{-1} for the K-Te/BP2000 cell. The majority of the reversible capacity is attributed to active materials Te via K-Te electrochemistry. The discharge capacities for the 2nd and 5th cycle drastically drop to 189.6 and 112.8 mAh g^{-1}, respectively, for S/BP2000 cathode, and 478.4 and 344.8 mAh g^{-1}, respectively for Se/BP2000 cathode. The rapid capacity decline for S/BP2000 and Se/BP2000 cathodes could be ascribed to the shuttle effect.[26] By contrast, Te/BP2000 cathode demonstrates superior capacities of 459.7 and 440 mAh g^{-1} for the 2nd and 5th cycle, respectively. As shown in Figure 2d–e, the Te/BP2000 cathode delivers remarkable rate capacities of 459.7, 408.1, 368.8, 350.2, 328.7, 289.0, 257.5, and 238.0 mAh g^{-1}, as the current density increases from 0.1 to 10 A g^{-1}, respectively. When the current density is set back to 1 A g^{-1}, the capacity of Te/BP2000 cathode is restored to 357.1 mAh g^{-1}. However, S/BP2000 and Se/BP2000 exhibit poor rate capacities of 189.6, 71.4, 36.4, 19.1, 8.6, 2.2, 1.7 mAh g^{-1} and 478.4, 292.9, 233.8, 175.4, 111.0, 20.9, 4.6, 2.7 mAh g^{-1}, respectively under the same condition. Additionally, capacity utilization is defined by dividing the reversible capacity by the corresponding theoretical value (1675 mAh g^{-1} for S, 675 mAh g^{-1}

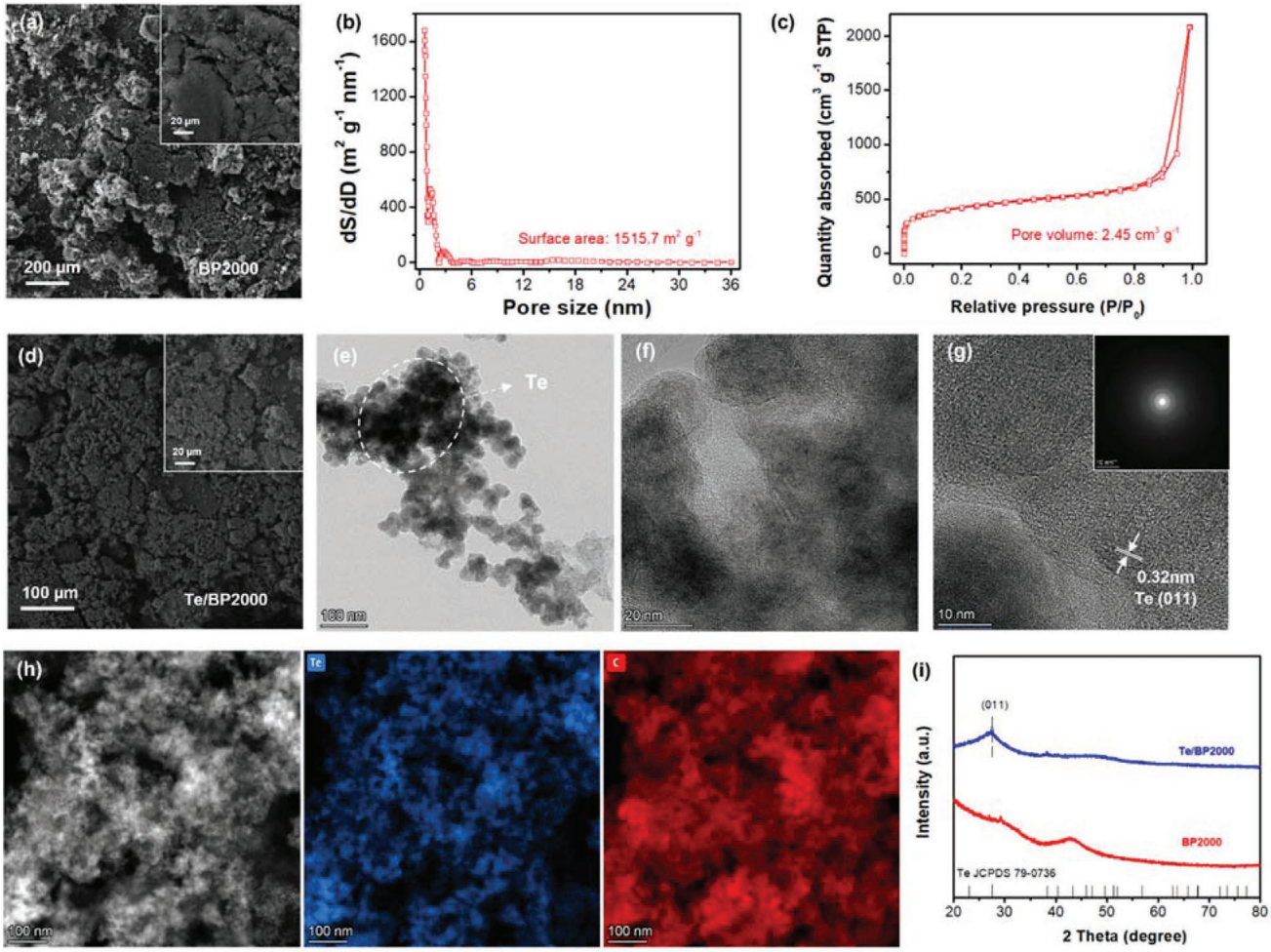

Figure 1. a) SEM image, b) pore size distribution, c) nitrogen adsorption–desorption isotherm of BP2000 porous carbon; d) SEM, e) TEM, f,g) HRTEM images of Te/BP2000 (the inset in (g)) is its corresponding SAED pattern), h) HAADF and elemental mapping of Te/BP2000, i) XRD patterns of BP2000 and Te/BP2000.

for Se, and 420 mAh g^{-1} for Te). It could be observed that Te/BP2000 has the highest capacity utilization of 97%, 88%, 83%, and 78% at 0.2, 0.5, 1, and 2 C, whereas S/BP2000 and Se/BP2000 display poor utilization of from 4% to 0.5% and from 43% to 16%, respectively. As the K-S/Se/Te batteries have the same cell configuration and undergo identical testing current and voltages, the superior rate performance and reversibility of Te/BP2000 could be contributed to the fast electron transfer due to Te's electrical conductivity. It should be noted that the S/BP2000 and Se/BP2000 cathode in this work could be further optimized by structural or electrolyte design.[27,42] The main point is that, with the help of fast electron transfer of Te, the redox kinetics in the K-Te system is boosted, thus illustrating better rate performance and higher capacity utilization, especially at high current densities. This K-Te battery can deliver a high capacity (420 mAh g_{Te}^{-1} or 2621 mAh cm_{Te}^{-3}) and an average potential of 1.3 V. Accordingly, the energy density of the K-Te battery can reach up to 546 Wh kg_{Te}^{-1} or 3407 Wh L_{Te}^{-1}. The low crustal abundance (0.001 mg kg^{-1}) of Te is a big challenge for the commercialization of Te-based batteries. Nevertheless, the recent U.S. Geological Survey indicates that the current tellurium reserve is sufficient and can satisfy the demand for Te for several decades.[43] The increasing demand for Te-based batteries could increase production and recycling technologies around Te and eventually reduce the material cost.[30]

To uncover the K-ion storage mechanism of Te, ex situ XRD and TEM tests are conducted to identify the phase compositions of Te/BP2000 cathodes at different discharge/charge states. As shown in **Figure 3**a, the charge/discharge profile possesses two voltage plateaus. Herein, XRD patterns of Te/BP2000 cathodes are collected when discharged to 1.3 and 0.5 V and charged to 1.9 and 3 V. Upon discharge to 1.3 V (point A), the diffraction peaks located at 33.6°, 38.8°, 44.8°, 53.3°, 54.5° are assigned to the (222), (102), (402), (042), and (060) planes of K_2Te_3 (JCPDS #71-0490). The noticeable diffraction rings in SAED (Figure 3b) can also be well indexed to (630), (301), and (803) crystal planes, and the lattice fringes of 0.32 and 0.29 nm in the HRTEM image (Figure 3e) correspond to the (221) and (411) planes of K_2Te_3. Upon further discharge to 0.5 V, the peaks at 23.9°, 30.2°, 39.3°, 41.5°, 44.5°, 53.3°, and 54.6° agree with the (301), (411), (600), (620), (541), (800), and (343) planes of K_5Te_3 (JCPDS #79-1056). Figure 3c,f also confirms the formation of

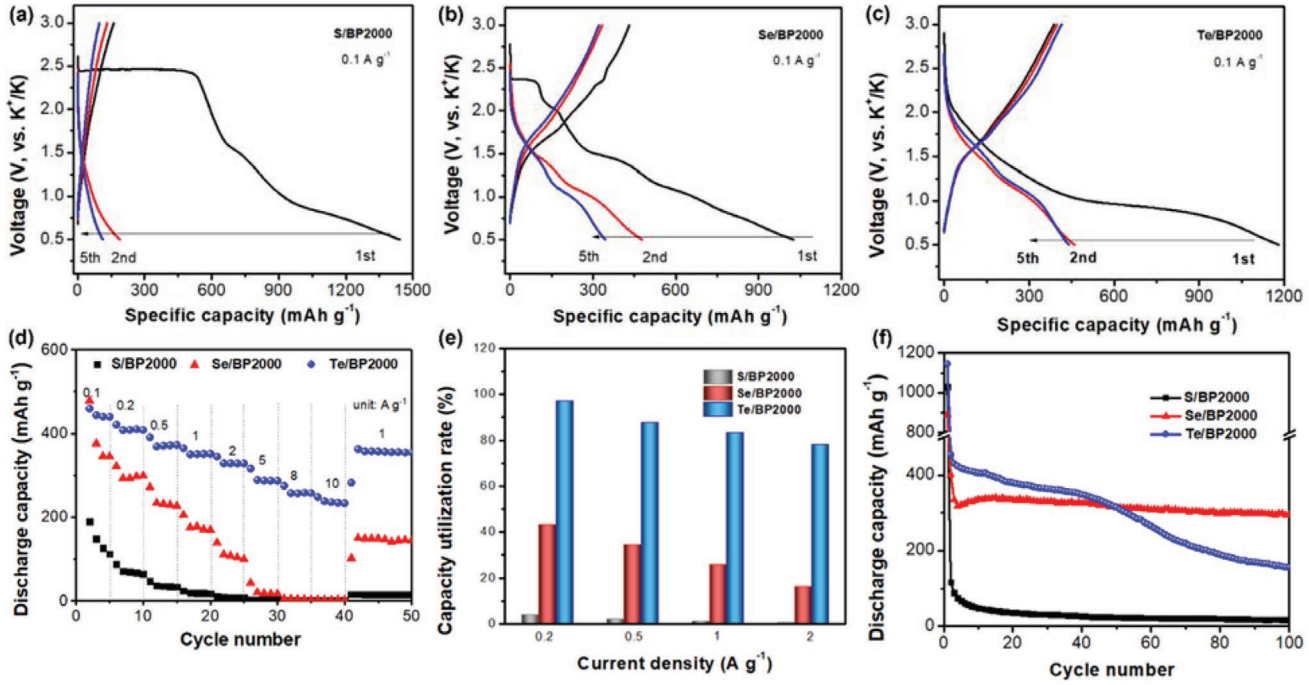

Figure 2. Charge–discharge profiles at initial cycles at 0.1 A g^{-1} for a) S/BP2000, b) Se/BP2000, c) Te/BP2000; d) rate capabilities, e) capacity utilization at 0.1–1 A g^{-1}, f) cycling performance of S/BP2000, Se/BP2000, and Te/BP2000 at 0.1 C (based on their own theoretical capacities).

K_2Te_3 by the diffraction rings originating from (305), (611), and (002) planes and lattice fringes of 0.68, 0.55, and 0.32 nm corresponding to (200), (001), (002) planes of K_2Te_3. Therefore, when the K-Te/BP2000 cell is discharged from 3 to 0.5 V, the Te phase is first converted to K_2Te_3 and finally discharged to K_5Te_3. For the charging process, K_2Te_3 is detected again as the cell is charged to 1.9 V. The newly appeared peaks at 27.5° and 38.3° when fully charged to 3 V are attributed to the (011) and (102) planes of Te (JCPDS #79-0736), indicating final charge product of Te. The SAED pattern and HRTEM image in Figure 3d,g furtherly support the generation of Te as the final charge product. Figure S5 (Supporting Information) demonstrates the uniform distribution of Te in the carbon host during the potassiation and depotassiation process. These observations reveal that the K-Te battery system experience a reversible two-step phase transformation from Te to K_2Te_3 and finally to K_5Te_3, as schematically illustrated in Figure 3h.

Our findings of the stepwise electrochemical conversion of Te are consistent with the ether-based K-Te battery at 0.5–3 V.[32] It should be noted that Guo et al.[35] claimed K_2Te as the most thermodynamically stable discharge product due to its lowest formation energy of –1.028 (versus –0.965 eV for K_5Te_3) when the K-Te cell is operated at 0.3–2.8 V. The reaction pathway in our work, from Te to K_2Te_3 and finally to K_5Te_3, is likely due to the higher cut-off voltage of 0.5–3 V.

A higher discharge voltage limit is also favorable since Te is used as cathode material in the K-Te battery system. Moreover, the pore structure is critical in affecting K-ion storage capacity and reaction pathways for K-Te batteries. Our group reported a Te/C cathode with activated carbon (ASAC25) as the Te host and this Te/ASAC25 cathode possessed only one pair of anodic/cathodic peaks in the same voltage range of 0.5–3 V,[36] suggesting a one-step electrochemical conversion from Te to K_2Te or K_5Te_3. This Te/ASAC25 showed stable cycling performance without significant capacity fading after 100 cycles at 0.2 C because of the effective Te confinement by highly microporous carbon. Unfortunately, this Te/ASAC25 electrode delivered poor rate capabilities with only about 150 mAh g^{-1} at 1 C, probably due to the low electrical conductivity of activated carbon. In contrast, BP2000 is more electrically conductive and presents superior rate performance. The rapid capacity decline possibly results from less effectiveness of mesopores than micropores in Te confinement, which was reported and discussed in the Li-Te batteries.[44] Therefore, it is necessary to introduce other strategies to stabilize the Te/BP2000 electrode and improve its structural integrity.

As discussed above, Te/BP2000 cathode delivers superior rate performance than S/BP2000 and Se/BP2000 due to its excellent electrical conductivity, despite a drastic capacity decline after 40 cycles. This capacity fading could be mainly ascribed to the significant volume expansion of Te when reacted with K-ion upon discharging.[35] To address this potential structural instability, one ultrathin aluminum oxide (Al_2O_3) layer is fabricated by atomic layer deposition (ALD). The thickness of the Al_2O_3 layer is precisely controlled to about 1 nm by manipulating 10 ALD cycles (TMA pulse/TMA purge/H_2O pulse/H_2O purge).[45] SEM images in **Figure 4**a,b show similar particle sizes of Te/BP2000 and Te/BP2000@$Al_2O_3$10. The brighter image of Te/BP2000@$Al_2O_3$10 is due to the SEM charging effect, suggesting the inferior electrical conductivity of the electrode surface due to the nonconductive Al_2O_3 layer. The strong signal of the Al element in the EDS spectra (Figure S6, Supporting Information) confirms the successful coating layer of Al_2O_3. Furtherly, Al 2s and 2p spectra are detected in the X-ray photoelectron spectroscopy

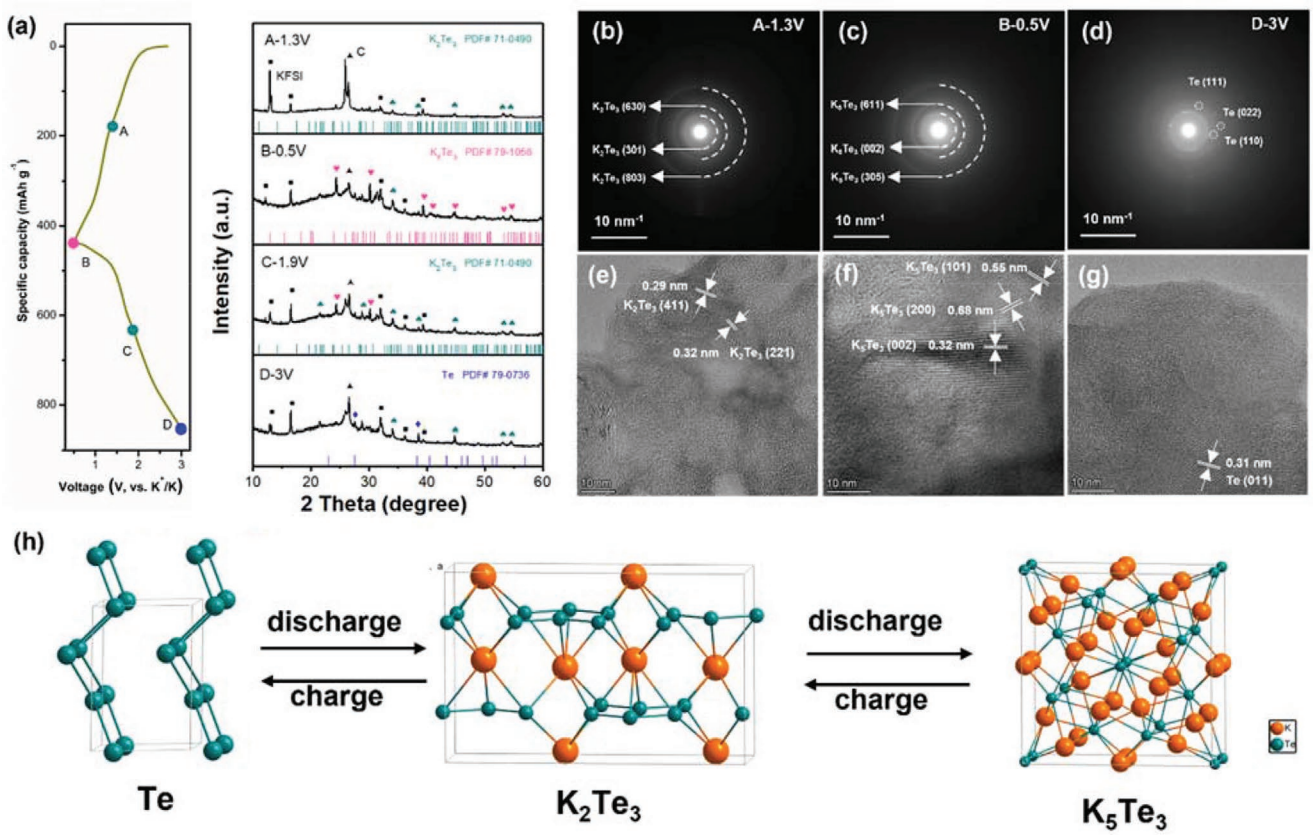

Figure 3. a) Galvanostatic charge–discharge profile of a K-Te battery and XRD patterns of Te/C electrodes at different charge/discharge states, b–d) SAED and e–g) HRTEM images for Te/C electrodes at different charge/discharge states, b,e) for 1.3 V, c,f) for 0.5 V, d,g) for 3 V, and h) phase transformation from Te to K_5Te_3.

(XPS) survey and high-resolution spectra, as illustrated in Figure 4c–d; and Table S1 (Supporting Information). The high-resolution Al 2p is decomposed into one prominent peak at 74.7 eV corresponding to the formation of Al—O bond,[46] which is verified by the peak located at 531.3 eV in O 1s spectra (Figure 4f). The Al peak is absent in Te/BP2000 (Figure 4e). XPS C1s and Te 3d spectra are demonstrated in Figure S7 (Supporting Information).

Furthermore, the Te/BP2000@$Al_2O_3$10 cathode exhibits a shoulder at 0.8 V on the first cathodic scan (Figure 4g) and lower discharge plateau in the first cycle (Figure 4h) compared to Te/BP2000. The slightly increased overpotential of Te/BP2000@$Al_2O_3$10 might be due to the elevated charge transfer resistance across the Al_2O_3-induced SEI layer.[47] The decreased initial discharge capacity possibly comes from suppressed side reactions by the unique SEI layer induced by Al_2O_3.[48] Based on these results, it can be concluded that the thin Al_2O_3 layer is successfully deposited on the Te/BP2000 electrode surface and is expected to confine active materials effectively and enhance the electrode's long-term structural stability.

The electrochemical performance of Te/BP2000 and Te/BP2000@$Al_2O_3$10 are evaluated and compared in K-Te cells with the cut-off voltage of 0.5–3 V. As shown in **Figure 5**a, the Te/BP2000 delivers a high initial capacity of 1145.8 mAh g^{-1} at 0.1 C, followed by a gradual decrease to 348.3 mAh g^{-1} in the 40th cycle. Afterward, the capacity drops dramatically and only retains 156.4 mAh g^{-1} after 100 cycles. In comparison, the Al_2O_3-coated Te/BP2000 cathode shows a slightly smaller capacity of 861.4 mAh g^{-1} in the first cycle. It maintains superior cycling stability with 300.9 mAh g^{-1} remaining after 100 cycles, twice the Te/BP2000 cathode. Figure 5b depicts Coulombic efficiency (CE) of Te/BP2000 and Te/BP2000@$Al_2O_3$10 cathodes over cycles. The Te/BP2000 cathode has a lower initial CE of 33.1% than Te/BP2000@$Al_2O_3$10 (41.3%), and the latter always displays higher CE than the former in the next 99 cycles. It could be speculated that Al_2O_3 induces the in situ generation of a more stable SEI layer to confine the active materials, accommodate the volume change of Te and passivate the electrode surface, thus enhancing the cycling stability of Te/BP2000 cathode. Moreover, an ether electrolyte-based K-Te battery was reported[32] to provide initial CEs of 40% and 60%, respectively, for 1 and 5 M KTFSI-in-DEGDME electrolytes. Our K-Te battery system with 1 M electrolyte showed comparable CE with this work. The as-mentioned improved CE in 5 M electrolyte can be explained by the fact that concentrated electrolyte effectively mitigates the dissolution of polytellurides and shuttle reactions. The rate capabilities of the two cathodes are also compared and shown in Figure 5c. As the current density increases from 0.1 to 5 C, Te/BP2000 and Te/BP2000@$Al_2O_3$10 cathodes deliver capacities of 454.2/437.8, 388.6/392.3, 359.6/362.5, 343.5/341.3, 320.9/314.9, and 291.1/286.5 mAh g^{-1}, respectively. The long-term cycling test at 1 C is also performed and illustrated in

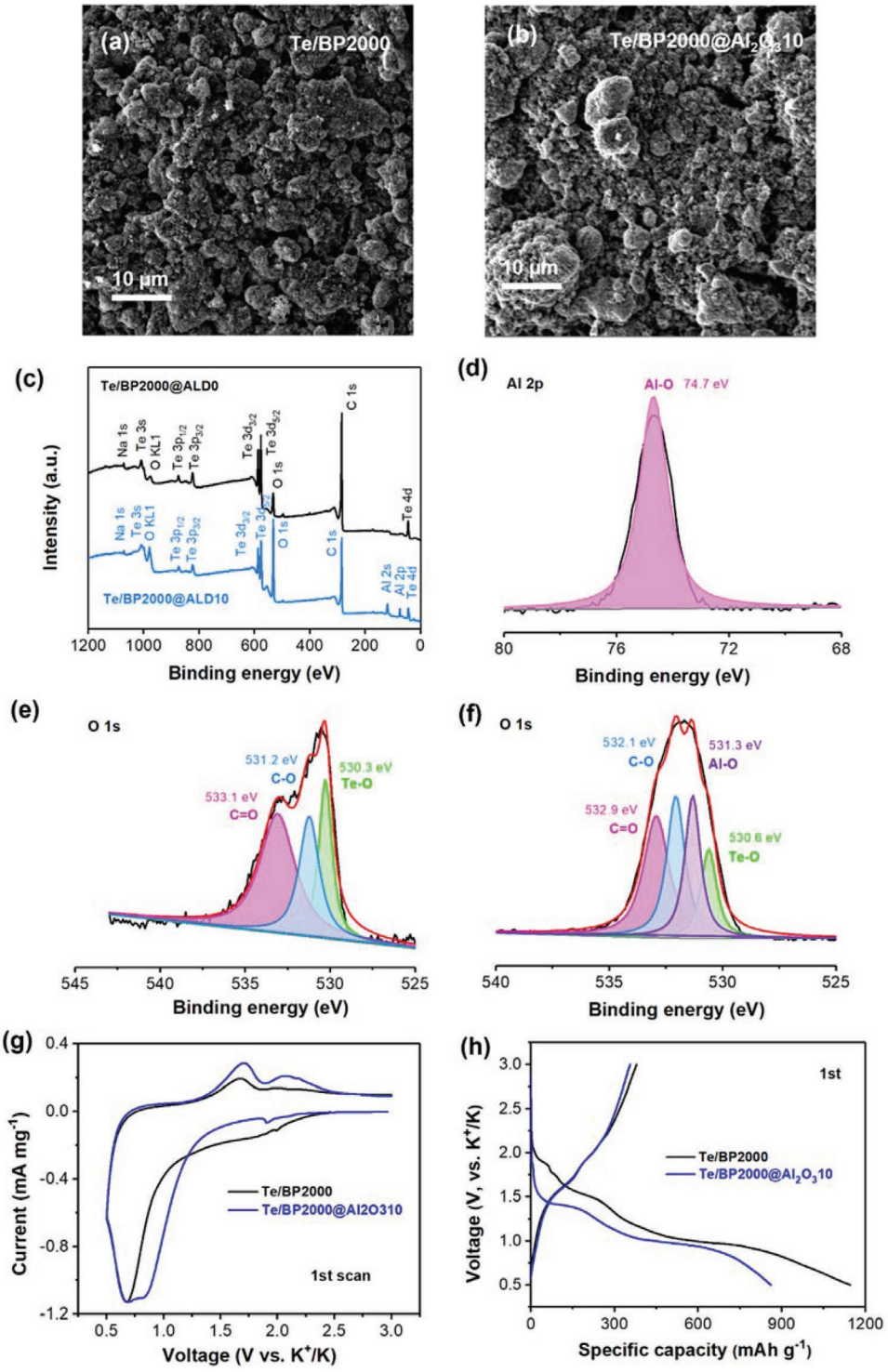

Figure 4. SEM images of a) Te/BP2000, b) Te/BP2000@$Al_2O_3$10, c) XPS survey, d) Al 2p spectra of Te/BP2000@$Al_2O_3$10, e,f) O 1s spectra of Te/BP2000 and Te/BP2000@$Al_2O_3$10, g) the first CV scan, h) the first charge/discharge profiles of Te/BP2000 and Te/BP2000@$Al_2O_3$10.

Figure 5d. The Al_2O_3-coated Te/BP2000 cathode demonstrates exceptional stability over 500 cycles and remains even 330.5 mAh g^{-1} with an ultralow capacity decay of only 0.01% per cycle. By contrast, the capacity of bare Te/BP2000 cathode steadily decreases versus repeated potassiation/depotassiation cycles, and its corresponding capacity decay is 0.04% per cycle. The excellent cyclability of Te/BP2000@$Al_2O_3$10 cathode could be attributed to the strengthened structural stability of the in-situ generated SEI layer resulting from the Al_2O_3 film. Figure 5f–g presents galvanostatic charge/discharge profiles of Te/BP2000 and Te/BP2000@$Al_2O_3$10 cathodes in the 2nd, 40th, and 80th cycles. It could be seen that, with cycle number

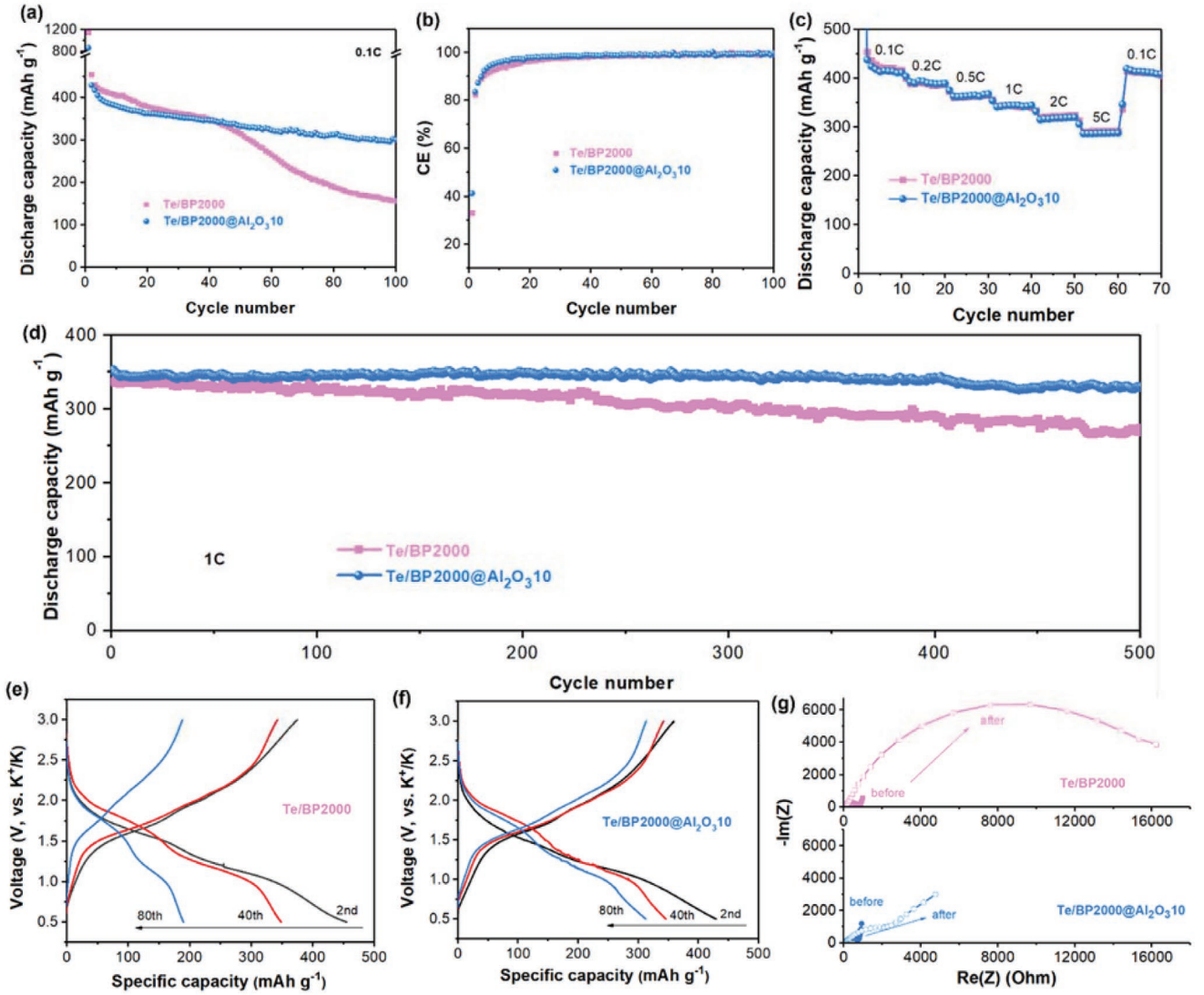

Figure 5. Electrochemical performance of Te/BP2000 and Te/BP2000@$Al_2O_3$10. a) Discharge capacity, b) Coulombic efficiency over 100 cycles at 0.1 C, c) rate performance, d) long-term cycling performance at 1 C, galvanostatic charge/discharge profiles of Te/BP2000 and Te/BP2000@$Al_2O_3$10 at 2nd, 40th, and 80th, g) EIS plot of Te/BP2000 and Te/BP2000@$Al_2O_3$10 before and after 100 cycles at 0.1 C.

increasing to 80, the discharge plateau of Te/BP2000 at around 1 V becomes narrower, implying the incomplete conversion from K_2Te_3 to K_5Te_3 or the loss of active materials. In comparison, the Al_2O_3-coated cathode delivers a wider discharge plateau at 1 V, ensuring that K_2Te_3 is completely converted to K_5Te_3. Figure 5g compares the EIS plots of Te/BP2000 and Te/BP2000@$Al_2O_3$10 cathodes before and after 100 cycles operated at 0.1 C. On the other hand, by electrochemical impedance spectroscopy (EIS) simulation using the equivalent model in Figure S8 (Supporting Information), the Te/BP2000@$Al_2O_3$10 cathode possesses a slightly higher charge transfer resistance R_{ct} than the bare Te/BP2000 cathode because it is difficult for electrons to pass through the insulating Al_2O_3 layer. After 100 cycles, the R_{SEI} and R_{ct} of Te/BP2000@$Al_2O_3$10 cathode are 133.3 and 801.8 Ω, respectively, whereas the Te/BP2000 cathode has significantly enlarged R_{SEI} and R_{ct} of 801.8 and 4.2E4 Ω. Two reasons could explain the markedly increased R_{SEI} and R_{ct} of Te/BP2000. First, Te active materials are gradually lost from the micro/mesopores of BP2000 due to large volume change, causing structural instability, pulverization, and isolation of active materials from the current collector. Second, the SEI layer on the surface of the Te/BP2000 electrode is repeatedly destroyed and rebuilt, resulting in drastically increased interfacial resistance. In contrast, the ultrathin Al_2O_3 film enables the in situ generated SEI layer to enhance structural integrity, confine Te effectively, and prevent active material loss over long-term cycles, extending the lifetime of Te/BP2000 with ultrahigh capacity retention as shown in Figure 5d.

To reveal the surface chemistry on the Te/BP2000 cathode, the cycled K-Te/BP2000 and K-Te/BP2000@$Al_2O_3$10 cells are disassembled for post characterizations. **Figure 6**a,b; and Figure S9 (Supporting Information) shows top-view and cross-sectional SEM images of K-Te/BP2000 and K-Te/BP2000@$Al_2O_3$10 electrodes after 100 cycles at 0.1 C. Some particles are separated from the surface of Te/BP2000, and a majority of active materials are peeled off from the Al current

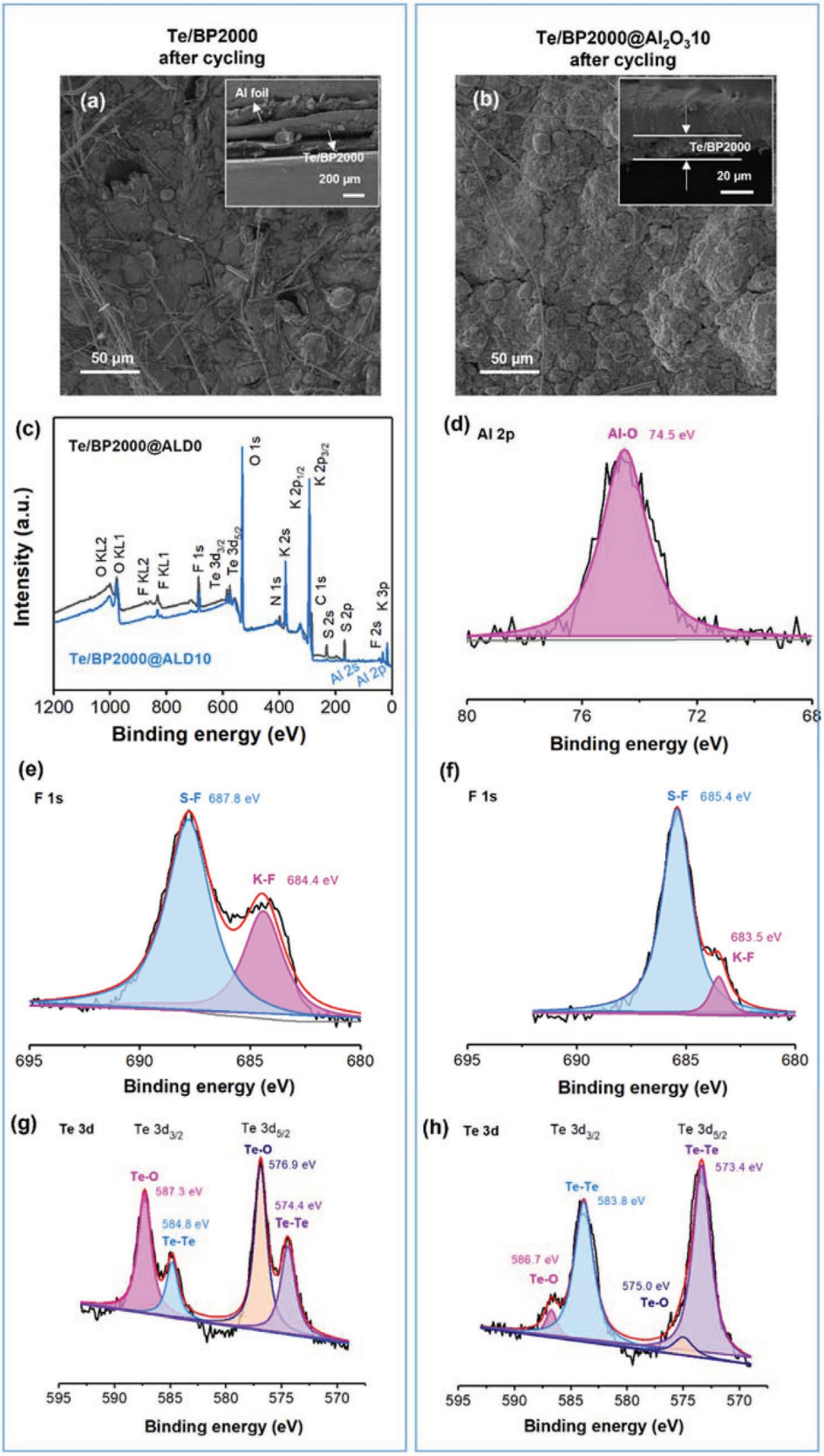

Figure 6. Top-view and cross-section SEM images of a) Te/BP2000 and b) Te/BP2000@$Al_2O_3$10 after 100 cycles, c) XPS survey spectra, d) Al 2p of Te/BP2000@$Al_2O_3$10, e,f) F 1s and g,h) Te 3d spectra of Te/BP2000 and b) Te/BP2000@$Al_2O_3$10 after cycling.

collector. The delamination causes the electrical isolation from Al foil, which explains the drastic capacity decline and enlarged interfacial resistance in Figure 5. Meanwhile, Te/BP2000@$Al_2O_3$10 active materials are firmly attached to the Al foil, ensuring efficient charge transfer and K-ion conduction. The XPS survey spectra in Figure 6c and prominent Al-O peak in Figure 6d confirm the existence of Al in the SEI layer on the Te/BP2000@$Al_2O_3$10 surface. K 2p, C 1s, and O 1s spectra are illustrated in Figure S10 (Supporting Information). The two peaks at 687.8 and 684.4 eV in F 1s (Figure 6e) are assigned to the S—F and K—F bonds for Te/BP2000,[11,49] which shift to 685.4 and 683.5 eV for cycled Te/BP2000@$Al_2O_3$10 (Figure 6f), respectively. The binding energy shift indicates different charge states of F, which might be caused by the interaction with Al. On the other hand, the intensities of Te—Te bonds are much more intense, and Te—O bonds become far weaker for Te/BP2000@$Al_2O_3$10 (Figure 6g) in Te 3d spectra than Te/BP2000 (Figure 6h), implying higher electrochemical activity of Te for the Al_2O_3-coated electrode. Based on the above results, it could be inferred that the Al_2O_3 film induces the formation of the KAl_xO_y-rich SEI layer, which effectively passivates the Te/BP2000 electrode and enhances its structural stability after long-term potassiation/depotassiation behaviors.[50]

Figure 7 illustrates the structural change of Te/BP2000 and Te/BP2000@$Al_2O_3$10 after long-term cycles based on the electrochemical performance and ex situ morphology or structural characterization results. For the bare Te/BP2000 cathode, the mesopores in the carbon host are pretty large and could not confine Te species effectively, resulting in pulverization and loss of active materials after long cycling. The delamination isolates Te species from the current collector, leading to drastically increased interfacial resistance and rapid capacity decline. In comparison, the deposited ultrathin Al_2O_3 film induces the generation of a stable SEI, which protects active materials from loss and enables fast electron transfer for complete electrochemical conversion from Te to K_5Te_3. It is speculated that 10-cycle ALD is likely to leave some small gaps on the surface of micropores and the ALD layer is effective to block the loss of large-size Te active materials inside micro/mesoporous carbon. Benefiting from the functional interface layer, the Te/BP2000@$Al_2O_3$10 delivers superior cling stability with 95% capacity retention at 1 C. On the other hand, the Al_2O_3 layer was also deposited on the surface of S/BP2000 and Se/BP2000 cathodes to investigate the effect of interface layer on S or Te potassiation/depotassiation behaviors. As shown in Figure S11 (Supporting Information), both S/BP2000@$Al_2O_3$10 and Se/BP2000@$Al_2O_3$10 delivered higher capacities after the deposition of 10 nm Al_2O_3,

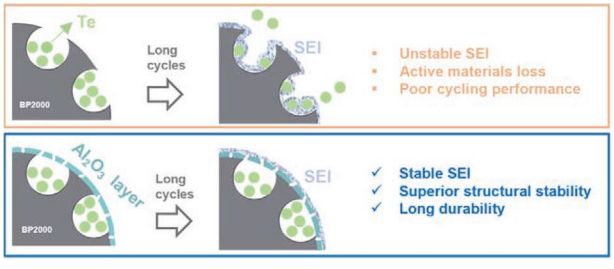

Figure 7. Schematic illustration of the structural change of Te/BP2000 and Te/BP2000@$Al_2O_3$10 after long-term cycles.

which furtherly confirms the effectiveness of the Al_2O_3 layer in stabilizing the cathode interface and preventing the loss of active materials. Therefore, ALD is an effective strategy to stabilize S/Se/Te cathode and electrolyte interface to enable durable and high-capacity K-chalcogen batteries.

3. Conclusions

In summary, Te/BP2000 has been demonstrated to deliver superior specific capacity and rate performance than its counterparts S/BP2000 and Se/BP2000 due to the significantly higher electrical conductivity of Te than S and Se. The K-ion storage mechanism of Te/BP2000 cathode in carbonate electrolytes was revealed with a stepwise phase transformation from Te to K_2Te_3 and ultimately to K_5Te_3 by XRD, HRTEM, and SAED analysis. Moreover, ultrathin Al_2O_3 film with 1 nm thickness was deposited on Te/BP2000 surface to induce a stable SEI layer and protect active materials from loss after long-term cycles. The Te/BP2000@$Al_2O_3$10 delivered highly reversible capacity over 500 cycles at 1 C with an ultralow capacity decay of only 0.01% per cycle, corresponding to 95% capacity retention. In contrast, the uncoated Te/BP2000 only maintains 80% of initial capacity after long-term cycling. The notably improved cycling stability and enhanced structural integrity can be attributed to the passivation of the Al_2O_3-induced SEI layer, which could effectively confine Te species, accommodate their volume change and prevent the loss of active materials. These findings provide feasible strategies for developing durable and high-rate K-Te batteries.

4. Experimental Section

Materials: Te powder (Fenix Advanced Materials, 99.99%), sulfur powder (Alfa Aesar, 100 mesh, 99.5%), Se powder (Sigma-Aldrich, 100 mesh, ≥ 99.5%), porous carbon (BP2000, CABOT Inc.), sodium alginate (SA, Ward's Science), potassium bis(fluorosulfonyl)imide (KFSI, Solvionic, CAS: 14984-76-0), ethylene carbonate (EC, Gotion, CAS: 96-49-1), and diethyl carbonate (DEC, Gotion, CAS: 105-58-8) were used as received. The precursors for ALD were tretrimethylaluminum (TMA) and deionized water (H_2O).

Preparation of Te/BP2000 Cathode: The Te/BP2000 composite was prepared by a conventional melt-diffusion method. Te and BP2000 powder at the mass ratio of 2:1 were mixed, fully ground, and then transferred to a ceramic boat, heated in a sealed glass tube at 550 °C for 6 h at a heating rate of 5° min^{-1} under continuous nitrogen flow. Te/BP2000 composite was obtained after cooling down to room temperature. Te/BP2000 composite was mixed thoroughly with super P and sodium alginate (2 wt% in aqueous solution) with a mass ratio of 7:2:1 to form a uniform slurry. Afterward, the slurry was cast onto an aluminum foil and dried at 80 °C in a vacuum oven overnight. Finally, the dried slurry was cut into 12 mm diameter pellets and used as Te/BP2000 cathodes for coin-cell assembly. Similarly, the S/BP2000 and Se/BP2000 composites were prepared by heating the mixture of S or Se and C at the mass ratio of 1:1 in an autoclave at 160 and 260 °C for 24 h. Subsequently, the S/BP2000 and Se/BP2000 cathodes were prepared following the same procedures as Te/BP2000 cathodes.

Atomic Layer Deposition of Al_2O_3 on Te/C Electrodes: The Al_2O_3 layer was coated on the Te/BP2000 cathodes via a commercial ALD reactor (GEMStar XT Atomic Layer Deposition Systems; Arradiance). The coating process was carried out at 100 °C by following a TMA pulse/TMA purge/H_2O pulse/H_2O purge sequence in each cycle. After 10 cycles,

Al_2O_3 films are deposited on Te/BP2000 cathodes noted as Te/BP2000@$Al_2O_3$10.

Materials Characterizations: The morphologies and microstructures of the Te/BP2000 composite powder and cathode were observed by scanning electron microscopy (SEM), transmission electron microscopy (TEM), and energy dispersive spectrometer (EDS). Thermogravimetric analysis (TGA) of S/Se/Te and BP2000 composite powder was operated at 30–800 °C in a nitrogen atmosphere to determine the S/Se/Te content. The nitrogen adsorption-desorption method was used to investigate the pore structure (pore volume, surface area, and pore size distribution) of BP2000. X-ray diffraction (XRD) was used to analyze the crystal structure of BP2000, Te/BP2000 composite powder, and Te/BP2000 cathodes after battery cycling. X-ray photoelectron spectroscopy (XPS) was used to collect surface composition information of bare and Al_2O_3-coated Te/BP2000.

Electrochemical Measurements: CR2032 cells were assembled in an argon-filled glovebox workstation with H_2O and O_2 less than 0.1 ppm. K metal was used as the counter electrode, and Te/BP2000 (S/BP2000 or Se/BP2000) electrode as the working electrode. Glass fiber (GF/D, Whatman) was employed as the separator with 200 µL electrolyte (1 M KFSI in EC: DEC) added in each cell. The galvanostatic charge–discharge tests were performed in 0.5–3 V in a constant current mode using a NEWARE battery cycler (CT-4008T-5V50 mA-164, Shenzhen, China). The specific capacity at 0.1–10 A g^{-1} of the Te/BP2000 (S/BP2000 or Se/BP2000) cathode was calculated based on the mass of Te (S or Se). The capacity utilization rate at each current density was defined as the ratio of delivered capacity to theoretical capacity (1675 mA g^{-1} for S, 675 mA g^{-1} for Se 420 mA g^{-1} for Te). The Te loading of the Te/C electrode was ≈1 mg cm^{-2}. Cyclic voltammetry (CV) test was conducted in the range of 0.5–3 V (vs K^+/K) at scan rates of 0.2 mV s^{-1}. The electrochemical impedance spectroscopy (EIS) test of K-Te cells with/without Al_2O_3 coating layer was carried out in a frequency range of 0.01–1 MHz with a voltage amplitude of 5 mV before and after cycling. The cycled K-Te batteries were disassembled in the argon-filled glove box and rinsed with the DEC solvent to remove electrolyte and salt residuals. After being dried in the glove box overnight, the electrodes were placed in a sealed bag for SEM, XRD, and XPS characterizations. To reveal potential reaction pathways in a K-Te cell, the K-Te/BP2000 cells at different charge/discharge states (0.5, 1.3, 1.9, 3 V) were disassembled, rinsed with DEC, and dried in a glovebox for XRD and TEM characterizations.

Supporting Information

Supporting Information is available from the Wiley Online Library or from the author.

Acknowledgements

This work was supported by the Mitacs Accelerate Program, Natural Sciences and Engineering Research Council of Canada (NSERC), Canada Foundation for Innovation (CFI), BC Knowledge Development Fund (BCKDF), Fenix Advanced Materials, and the University of British Columbia (UBC). The authors would like to thank Dr. Carmen Andrei at the Canadian Centre for Electron Microscopy (CCEM) at McMaster University for her help on electron microscopy characterization, Dr. Aruhan at UBC for his help in illustrating phase transformation of Te, and Dr. Sudip Shrestha at the UBC Fipke Laboratory for Trace Element Research (FiLTER) for providing support for SEM and EDS analysis. The authors declare that they have no known competing financial interests or personal relationships that could have appeared to influence the work reported in this paper.

Conflict of Interest

The authors declare no conflict of interest.

Data Availability Statement

The data that support the findings of this study are available in the Supporting Information of this article.

Keywords

atomic layer deposition, potassium-tellurium batteries, solid electrolyte interphases, structural stability, tellurium/carbon electrodes

Received: January 5, 2022
Revised: January 29, 2022
Published online:

[1] F. Ding, W. Xu, G. L. Graff, J. Zhang, M. L. Sushko, X. Chen, Y. Shao, M. H. Engelhard, Z. Nie, J. Xiao, X. Liu, P. V. Sushko, J. Liu, J. G. Zhang, *J. Am. Chem. Soc.* **2013**, *135*, 4450.
[2] Y. Ding, Z. P. Cano, A. Yu, J. Lu, Z. Chen, *Electrochem. Energy Rev.* **2019**, *2*, 1.
[3] A. Manthiram, *ACS Cent. Sci.* **2017**, *3*, 1063.
[4] J. B. Goodenough, Y. Kim, *Chem. Mater.* **2010**, *22*, 587.
[5] T. P. Narins, *Extr. Ind. Soc.* **2017**, *4*, 321.
[6] T. C. Wanger, *Conserv. Lett.* **2011**, *4*, 202.
[7] A. Eftekhari, Z. Jian, X. Ji, *ACS Appl. Mater. Interfaces* **2017**, *9*, 4404.
[8] H. Kim, J. C. Kim, M. Bianchini, D.-H. Seo, J. Rodriguez-Garcia, G. Ceder, *Adv. Energy Mater.* **2018**, *8*, 1702384.
[9] X. Zhang, Z. Wei, K. N. Dinh, N. Chen, G. Chen, F. Du, Q. Yan, *Small* **2020**, *16*, 2002700.
[10] W. Zhang, Z. Wu, J. Zhang, G. Liu, N.-H. Yang, R.-S. Liu, W. K. Pang, W. Li, Z. Guo, *Nano Energy* **2018**, *53*, 967.
[11] H. Wang, D. Yu, X. Wang, Z. Niu, M. Chen, L. Cheng, W. Zhou, L. Guo, *Angew. Chem., Int. Ed. Engl.* **2019**, *58*, 16451.
[12] Y. Li, L. Zhang, S. Liu, X. Wang, D. Xie, X. Xia, C. Gu, J. Tu, *Nano Energy* **2019**, *62*, 367.
[13] Y. Li, L. Zhang, J. Zhang, X. Wang, C. Gu, X. Xia, J. Tu, *Adv. Energy Mater.* **2021**, *11*, 2100470.
[14] C. Wei, Y. Tao, H. Fei, Y. An, Y. Tian, J. Feng, Y. Qian, *Energy Storage Mater.* **2020**, *30*, 206.
[15] Q. Zhang, Z. Wang, S. Zhang, T. Zhou, J. Mao, Z. Guo, *Electrochem. Energy Rev.* **2018**, *1*, 625.
[16] A. Eftekhari, *J. Power Sources* **2004**, *126*, 221.
[17] H. Kim, J. C. Kim, S.-H. Bo, T. Shi, D.-H. Kwon, G. Ceder, *Adv. Energy Mater.* **2017**, *7*, 1700098.
[18] C. Vaalma, G. A. Giffin, D. Buchholz, S. Passerini, *J. Electrochem. Soc.* **2016**, *163*, A1295.
[19] T. Hosaka, T. Shimamura, K. Kubota, S. Komaba, *Chem. Rec.* **2019**, *19*, 735.
[20] Y. Chen, W. Luo, M. Carter, L. Zhou, J. Dai, K. Fu, S. Lacey, T. Li, J. Wan, X. Han, Y. Bao, L. Hu, *Nano Energy* **2015**, *18*, 205.
[21] L. Fan, R. Ma, J. Wang, H. Yang, B. Lu, *Adv. Mater.* **2018**, *30*, 1805486.
[22] X. Wu, D. P. Leonard, X. Ji, *Chem. Mater.* **2017**, *29*, 5031.
[23] X. L. Huang, Z. Guo, S. X. Dou, Z. M. Wang, *Adv. Funct. Mater.* **2021**, *31*, 2102326.
[24] S. Lee, J. Lee, J. Kim, M. Agostini, S. Xiong, A. Matic, J.-Y. Hwang, *Energies* **2020**, *13*, 2791.
[25] Q. Yao, C. Zhu, *Adv. Funct. Mater.* **2020**, *30*, 2005209.
[26] Q. Liu, W. Deng, Y. Pan, C. F. Sun, *Chem. Sci.* **2020**, *11*, 6045.
[27] H. Huang, X. Luo, Y. Yao, X. Zhou, Y. Jiang, C. Guo, J. Liu, X. Wu, Y. Yu, *InfoMat* **2021**, *3*, 421.
[28] J. Ding, H. Zhang, W. Fan, C. Zhong, W. Hu, D. Mitlin, *Adv. Mater.* **2020**, *32*, 2070174.

[29] X. Huang, J. Sun, L. Wang, X. Tong, S. X. Dou, Z. M. Wang, *Small* **2021**, *17*, 2004369.
[30] Y. Zhang, D. Manaig, D. J. Freschi, J. Liu, *Energy Storage Mater.* **2021**, *40*, 166.
[31] Z. Chen, Y. Zhao, F. Mo, Z. Huang, X. Li, D. Wang, G. Liang, Q. Yang, A. Chen, Q. Li, *Small Struct.* **2020**, *1*, 2000005.
[32] Q. Liu, W. Deng, C.-F. Sun, *Energy Storage Mater.* **2020**, *28*, 10.
[33] N. Ding, S.-F. Chen, D.-S. Geng, S.-W. Chien, T. An, T. S. A. Hor, Z.-L. Liu, S.-H. Yu, Y. Zong, *Adv. Energy Mater.* **2015**, *5*, 1401999.
[34] T. Koketsu, B. Paul, C. Wu, R. Kraehnert, Y. Huang, P. Strasser, *J. Appl. Electrochem.* **2016**, *46*, 627.
[35] S. Dong, D. Yu, J. Yang, L. Jiang, J. Wang, L. Cheng, Y. Zhou, H. Yue, H. Wang, L. Guo, *Adv. Mater.* **2020**, *32*, 1908027.
[36] Y. Zhang, C. Liu, Z. Wu, D. Manaig, D. J. Freschi, Z. Wang, J. Liu, *ACS Appl. Mater. Interfaces* **2021**, *13*, 16345.
[37] J. U. Seo, G. K. Seong, C. M. Park, *Sci. Rep.* **2015**, *5*, 7969.
[38] Y. Liu, J. Wang, Y. Xu, Y. Zhu, D. Bigio, C. Wang, *J. Mater. Chem. A* **2014**, *2*, 12201.
[39] L. Zhou, Y. Cui, D. Kong, W. Feng, X. Gao, Y. Yan, H. Ren, H. Hu, Q. Xue, Z. Yan, W. Xing, *J. Energy Chem.* **2021**, *61*, 319.
[40] Y. Liu, W. Wang, J. Wang, Y. Zhang, Y. Zhu, Y. Chen, L. Fu, Y. Wu, *Chem. Commun.* **2018**, *54*, 2288.
[41] Y. Liu, Z. Tai, Q. Zhang, H. Wang, W. K. Pang, H. K. Liu, K. Konstantinov, Z. Guo, *Nano Energy* **2017**, *35*, 36.
[42] C. Ye, J. Shan, D. Chao, P. Liang, Y. Jiao, J. Hao, Q. Gu, K. Davey, H. Wang, S. Z. Qiao, *J. Am. Chem. Soc.* **2021**, *143*, 16902.
[43] N. T. Nassar, T. E. Graedel, E. Harper, *Sci. Adv.* **2015**, *1*, e1400180.
[44] Y. Zhang, W. Lu, P. Zhao, M. H. Aboonasr Shiraz, D. Manaig, D. J. Freschi, Y. Liu, J. Liu, *Carbon* **2021**, *173*, 11.
[45] K. Kaliyappan, J. Liu, B. Xiao, A. Lushington, R. Li, T.-K. Sham, X. Sun, *Adv. Funct. Mater.* **2017**, *27*, 1701870.
[46] M. Yu, W. Yuan, C. Li, J.-D. Hong, G. Shi, *J. Mater. Chem. A* **2014**, *2*, 7360.
[47] X. Zhang, I. Belharouak, L. Li, Y. Lei, J. W. Elam, A. Nie, X. Chen, R. S. Yassar, R. L. Axelbaum, *Adv. Energy Mater.* **2013**, *3*, 1299.
[48] C. Luo, H. Zhu, W. Luo, F. Shen, X. Fan, J. Dai, Y. Liang, C. Wang, L. Hu, *ACS Appl. Mater. Interfaces* **2017**, *9*, 14801.
[49] Q. Zhang, J. Mao, W. K. Pang, T. Zheng, V. Sencadas, Y. Chen, Y. Liu, Z. Guo, *Adv. Energy Mater.* **2018**, *8*, 1703288.
[50] W. Liu, P. Liu, D. Mitlin, *Adv. Energy Mater.* **2020**, *10*, 2002297.